Insight into interlayer magnetic coupling in 1*T*-type transition metal dichalcogenides based on the stacking of nonmagnetic atoms

Wenxuan Zhu, Cheng Song,* Yongjian Zhou, Qian Wang, Hua Bai, and Feng Pan†
Key Laboratory of Advanced Materials (MOE), School of Materials Science and Engineering, Tsinghua University, Beijing 100084, China

(Received 26 February 2021; accepted 24 May 2021; published 1 June 2021)

The interlayer coupling in two-dimensional (2D) magnetic materials is significantly important in determining the properties of 2D materials and applications of related devices. However, the mechanism that determines the interlayer magnetic coupling has only been comprehensively studied in CrI_3 and that of transition metal dichalcogenides is still blurred. In this work, through first-principle calculations, we find in 2D magnetic bilayer that the interlayer magnetic coupling is determined by the stacking order of interlayer nonmagnetic atoms, accompanied by the transition between half metal and semiconductor in MnS_2. The nonmagnetic atoms bridge the interlayer coupling and the stacking order of nonmagnetic atoms determines the interlayer coupling by altering the interlayer p_z-orbital bonding. Adjusting the structure of interlayer nomagnetic atoms by biaxial strain can also tune the interlayer coupling. The perspective proposed in our work, from the stacking order of nonmagnetic atoms, to understand the interlayer magnetic coupling is also applicable in other 2D materials.

DOI: 10.1103/PhysRevB.103.224404

I. INTRODUCTION

The family of two-dimensional(2D) materials combined by van der Waals (vdW) force between layers is growing rapidly [1,2] and 2D magnets have gradually developed into an important branch since its experimental realization [3,4]. Due to the weak interlayer coupling of 2D magnets, abundant methods are able to efficiently control the interlayer magnetic coupling. Representatively, in 2D antiferromagnet CrI_3, electric gating [5,6] and magnetic field [7,8] have been utilized to control the interlayer coupling, which leads to the giant tunneling magnetoresistance. The exploration of key factors that determine the interlayer magnetic coupling has significance for the design of spintronic devices [9] composed of 2D magnets. Generally, the interlayer coupling is considered to be different from intralayer superexchange. However, because of the difference in interlayer interaction, the mechanism in a specific system still needs to be revealed.

The weak interlayer vdW force also makes 2D materials feasible to be constructed into stacking [10], which influences various properties of the material [11]. By stacking two atomic layers into moiré structure, interesting properties including superconductivity [12,13], moiré excitons [14,15], and the quantum anomalous Hall effect [16] have been realized [17] and the combination of different materials [18] can achieve the superposition of various properties, such as the quantum anomalous Hall effect [19], the topological superconductivity [20], multiferroicity [21], etc. Especially, the effect of stacking is particularly predominant in 2D magnetic materials [3,4,22]. Recently, stacking order was also found to be an efficient method to regulate the interlayer coupling in CrI_3, which possesses two phases with different stacking orders [23]. Both high pressure [24,25] and molecular-beam epitaxy growth [26] are able to alter the stacking order by translational and rotational transformation. From study of the stacking tunable interlayer coupling, the interlayer coupling in CrI_3 was found to be influenced by the interlayer p_{xy}–p_z orbital hybridization of I atoms [27,28]. Therefore, the function of bridging the magnetic coupling and structure makes diverse stacking order an effective perspective to understand the interlayer coupling. However, the stacking tunable interlayer coupling has only been studied in 2D magnets which have similar structures as CrX_3 (X = Cl, Br, I) [27–30], possessing Curie temperature far below room temperature. The effect of stacking ordering on interlayer coupling and the mechanism of interlayer coupling is revealed in room-temperature 2D magnets, transition metal dichalcogenides (TMDs) [18], the structure of which is different from CrX_3 with interlayer charge distribution, remains to be investigated.

In our first-principle calculation work, we fill the gap of stacking tunable interlayer coupling in TMDs and extract the mechanism that determines the interlayer coupling. We mainly take 1*T*-phase MnS_2 (1*T*-MnS_2) bilayer as the research object. 1*T*-MnS_2 monolayer possesses intralayer ferromagnetic coupling, out-of-plane easy axis, and Curie temperature near room temperature [31,32], which is favorable by spintronic devices. However, only MnS_2 monolayer has been investigated in detail. By taking both translational and rotational transformations into account to construct different stacking order, we find the interlayer orbital hybridization which decides the interlayer coupling in 1*T*-MnS_2 is distinct from that of CrX_3 and $CrSe_2$ as proposed before [27,28,33] and the stacking order of interlayer nonmagnetic atoms rather than that of magnetic atoms [27,30,34] plays the dominant role in the determination of interlayer magnetic coupling in 2D magnets. Analyzing the interlayer coupling from the

*songcheng@mail.tsinghua.edu.cn
†panf@mail.tsinghua.edu.cn

perspective of nonmagnetic-atom stacking proposed in our work can also be applied to materials with other space groups and heterostructures composed of both magnetic and nonmagnetic layers. Accompanied by the conversion from interlayer ferromagnetic to antiferromagnetic coupling, a transition from half metal to semiconductor is also observed. In addition, changing the interlayer Mn–S …S–Mn bond angle by biaxial strain can also tune the interlayer coupling. Our work not only provides a perspective to understand the interlayer coupling in 2D magnets, but also demonstrates abundant spintronic properties in 1T-MnS_2.

II. METHODS

All the calculations are performed in the Vienna *Ab initio* Simulation Package (VASP) [35], with the Perdew-Burke-Ernzerhof functional [36]. The calculations were based on cutoff energy of 500 eV, which is large enough to converge the calculation (demonstrated in Supplemental Material, Fig. S1 [37]). Density-functional theory-D3, which can save the calculation time and provides a lattice constant in good agreement with the experiments, was used to properly treat the interlayer van der Waals interaction in both bulk and thin films [38]. The results with other vdW corrections are shown in Supplemental Material, Fig. S3. The generalized-gradient approximation with on-site Coulomb interaction (GGA+U) method was used to treat localized 3d orbitals; the U_{eff} is selected to be 3.9 and 1 eV for the 3d orbitals of Mn and Cr, respectively, according to previous studies [31,39–41]. The calculations based on different U_{eff} values are presented in Supplemental Material, Fig. S9 [37]. The tetrahedron method with Blöchl corrections was used in the calculations of total energy and differential charge density. The methods of Gaussian smearing with $\sigma = 0.02$ and with $\sigma = 0.002$ were used in the calculations of structure relaxation and band structure, respectively. The structures of antiferromagnetic coupling and ferromagnetic coupling are both optimized separately with both lattice constants and atom positions fully relaxed, using a force criterion of 0.01 eV/Å. The Gamma-centered k-point mesh of 12×12×1 and 9×9×1 were used in the calculations of MnS_2 and $Cr_2Ge_2Te_6$ (CGT), respectively. A vacuum layer larger than 15 Å was adopted in all calculations of thin films, which is large enough for the bilayer (demonstrated in Supplemental Material, Fig. S11 [37]).

Calculations of energy difference were based on the primitive cell with one Mn atom per layer in MnS_2 and two Cr atoms per layer in CGT, respectively, as highlighted by black dotted rhombuses in Figs. 1(a) and 5(a). The convergence precision of the total energy calculations was 1×10^{-7} eV. The magnetic anisotropy determined by calculating the energy difference between the magnetic moments aligned (001) and (100) including the spin-orbit coupling and the shape anisotropy due to magnetic dipolar interaction [42] was also considered (Supplemental Material [37]). The differential charge densities were obtained by comparing the total charge density between the bilayer and two individual layers. For biaxial strain modulation, the strains were applied in xy plane by expanding the lattice constant of equilibrium structure a_0 to $a_0 + \Delta a$. The strain was defined as $\varepsilon = \Delta a/a_0$. The atoms of all structures with strains are fully relaxed, using a force criterion of 0.01 eV/Å.

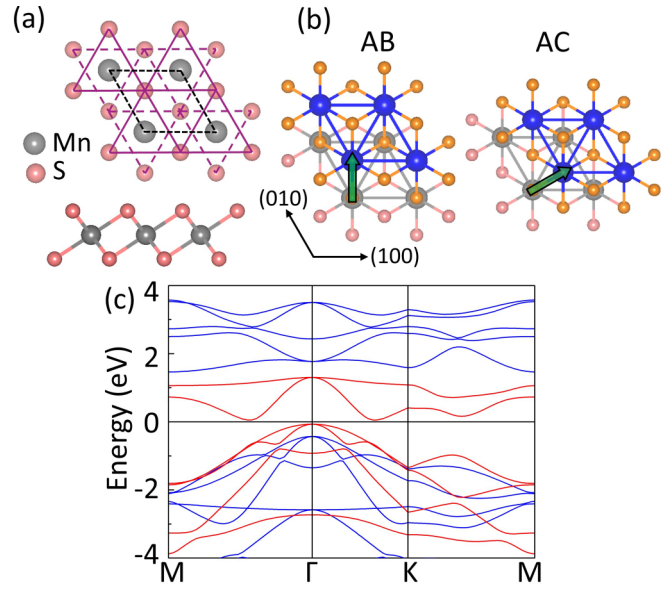

FIG. 1. Structure and band structure of MnS_2. (a) Top view and side view of monolayer MnS_2. The black dotted rhombuses highlight the primitive cell. (b) Top view of MnS_2 bilayer in AB stacking and AC stacking. Blue (gray) and orange (pink) balls represent Mn atoms and S atoms from top (bottom) layer. The green arrows represent the direction of translation. (c) Band structure of monolayer MnS_2, both spin-up (red) and spin-down (blue) bands are exhibited.

III. RESULTS AND DISCUSSION

1T-MnS_2 monolayer takes $P\bar{3}1m$ space group with Mn–S–Mn bond angle near 90°, generating intralayer ferromagnetic (FM) coupling by the superexchange of Mn–S–Mn. The structure of monolayer MnS_2 is shown in Fig. 1(a). Compared to most magnetic transition metal dichalcogenides with tetragonal symmetry and one layer per unit cell (1T-TMDs), which have in-plane easy axis, such as VSe_2 [43] and $CrTe_2$ [44], the easy axis of MnS_2 is out of plane. The basic properties of the monolayer are shown in Table I, which is consistent with previous theoretical work [31,32]. From the calculation of the band structure illustrated in Fig. 1(c), the monolayer MnS_2 is half metallic, with metallic spin-up channel and semiconducting spin-down channel. According to the symmetry and structure of MnS_2 monolayer, (1/3, 2/3, 0) and (2/3, 1/3, 0) are two high-symmetric positions as shown in Fig. 1(b). Therefore, by aligning the top layer with the bottom layer or shifting the top layer to (1/3, 2/3, 0) and (2/3, 1/3, 0),

TABLE I. Results of lattice constant a_0, Mn–S–Mn bond angle $\theta_{\text{Mn-S-Mn}}$, exchange energy per unit cell $E_{\text{ex}}(= E_{\text{FM}}–E_{\text{AFM}})$, magnetic moment of Mn M, and anisotropy energy magnetic anisotropy energy (MAE) ($E_{100}–E_{001}$).

	a_0 (Å)	$\theta_{\text{Mn-S-Mn}}$	E_{ex}(meV)	M (μ_B)	MAE ($E_{100}–E_{001}$) (μeV)
MnS_2	3.47	92.7	–98	3.7	43

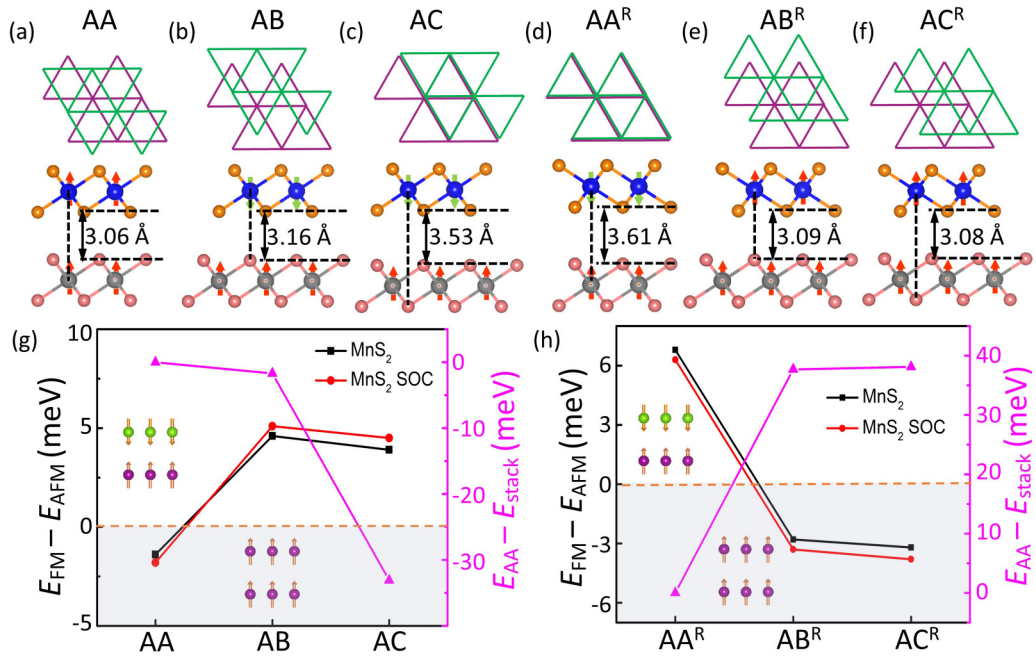

FIG. 2. Stacking-dependent interlayer coupling in MnS_2. (a)–(f) Structure of interlayer S atoms and side view of bilayer in different stacking orders (a)–(c) and after rotation (d)–(f). The green and magenta triangles represent the lower S atoms from top layer and the upper S atoms from bottom layer, respectively. Red and green arrows represent the magnetic moments of Mn atoms. The interlayer distance of the ground magnetic state is also shown. (g) Interlayer coupling energy defined as the difference between interlayer ferromagnetic coupling and antiferromagnetic coupling E_{FM}–E_{AFM} and stacking energy defined as the energy difference between AA stacking and particular stacking order E_{AA}–E_{stack} under different stacking orders. (h) Interlayer coupling energy and stacking energy under different stacking orders with rotational transform.

we achieve three bilayer configurations with different stacking orders, named as AA, AB, and AC, respectively .

Side views of different stacking orders are illustrated in Figs. 2(a)–2(c), in which the interlayer distance of the ground magnetic are shown. The interlayer distance with different interlayer coupling is shown in Supplemental Material, Table S1 [37]. From the comparison of the total energy in AA, AB, and AC, we find the energy difference between different stacking orders is small. Comparing the total energy with different interlayer magnetic coupling, it is clearly shown that MnS_2 bilayer experiences the attenuation of ferromagnetic coupling and the enhancement of antiferromagnetic coupling when the stacking order is changed from AA to AB and AC in Fig. 2(g), indicating stacking-dependent interlayer magnetic coupling. We then take both rotational and translational transformations into account at the same time. The top layer is rotated 180° around the Mn site relative to the bottom layer and then shifted to the AB and AC stacking order, as illustrated above. Different stacking orders after rotation are named as AA^R, AB^R, and AC^R. Interestingly, after rotation, as exhibited in Fig. 2(h), AA^R stacking favors antiferromagnetic coupling while AB^R and AC^R are ferromagnetic coupled, which is opposite to the results without rotational transformation. Also visible in Figs. 2(g) and 2(h) is that the emergence of spin-orbit coupling has a negligible effect on the interlayer coupling energy defined as E_{FM}–E_{AFM}. We also get similar results in $MnSe_2$ bilayer as discussed in Supplemental Material [37]. The rotational transformation alters the structure of interlayer S atoms and keeps the stacking order of Mn atoms unchanged. Figures 2(a)–2(c) show the stacking structure of interlayer S atoms in AA, AB, and AC, respectively. The stacking structures of interlayer S atoms in AA^R, AB^R, and AC^R are exhibited in Figs. 2(d)–2(f). AC stacking and AA^R stacking both possess antiferromagnetic coupling; their interlayer S atoms also have similar stacking structure, in which the lower S atoms from the top layer locate right above the upper S atoms from the bottom layer, as shown in Figs. 2(c) and 2(d). In contrast, AA stacking and AB^R both favor ferromagnetic coupling with similar interlayer structure of S atoms, in which the upper S atoms from bottom layer occupy the center of the triangle formed by the lower S atoms from the top layer as illustrated in Figs. 2(a) and 2(e).

Taking both translation and rotation into consideration, we create three stacking orders AA^R, AB^R, and AC^R which have not been theoretically studied before. Although the Mn atoms in AA and AA^R have similar stacking order, which is the ones from the top layer locating right above the ones from the bottom layer, resulting in the same amount of interlayer nearest-neighbor exchange and second-nearest-neighbor exchange interaction between Mn atoms, they possess opposite interlayer coupling. In contrast, in AC and AA^R, although the stacking of their Mn atoms is different, leading to different interlayer exchange interaction between Mn atoms, the stacking of their interlayer S atoms is the same, and so is their interlayer coupling. The similar condition is found in other stacking orders. Therefore, through the analysis of the obtained results, we come to the conclusion from a different perspective from previous work [27,30] that the interlayer coupling is able to be determined by the stacking order of interlayer nonmagnetic atoms alone. The results are checked

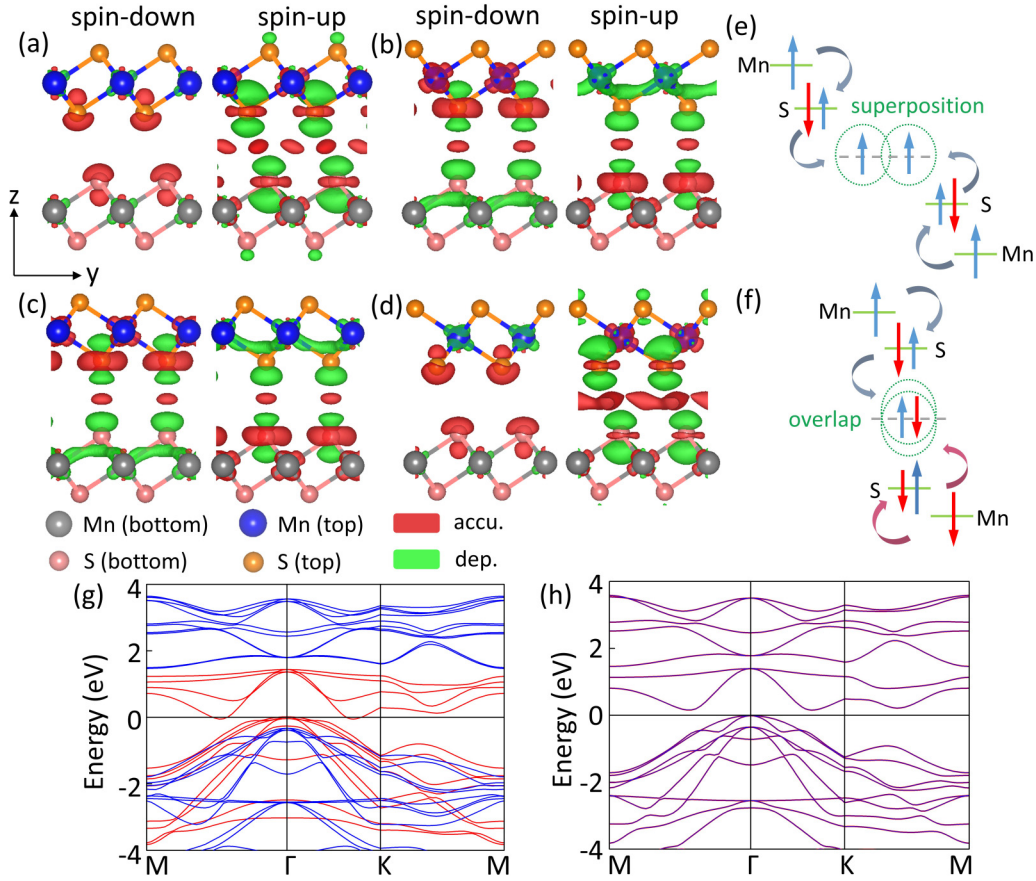

FIG. 3. DCD, interlayer exchange mechanism, and band structure of MnS_2 in different stacking. (a)–(d) Spin-dependent DCDs of MnS_2 in (a) AA, (b) AC stacking, (c) AA^R stacking, and (d) AB (isosurface value of $0.0001e/\text{bohr}^3$). Left and right DCDs in each figure represent spin-down and spin-up component, respectively. Red and green isosurface contours correspond to charge accumulation and depletion. Blue (gray) and orange (pink) balls represent Mn atoms and S atoms from top (bottom) layer. (e), (f) Interlayer coupling mechanism of (e) AA stacking and (f) AC stacking. (g), (h) Band structure of (g) AA and (h) AA^R stacking. Both spin-up (red) and spin-down (blue) bands are exhibited; degenerated bands are shown in purple.

with different methodologies in Supplemental Material [37]. Following the above guideline on the relationship between stacking order of nonmagnetic atoms and interlayer coupling, we construct $MnS_2/MoS_2/MnS_2$ heterostructures by inserting a 2D nonmagnetic MoS_2 layer between two MnS_2 layers with specific stacking orders and the expected magnetic configuration is obtained (Supplemental Material, Fig. S2 [37]). The out-of-plane easy axis persists in different stacking orders described above, suggesting the easy axis is insensitive to the stacking order (Supplemental Material, Table S2 [37]). The magnetic orders discussed above are proved to be the ground state in Supplemental Material.

Then we calculate the spin-dependent differential charge density (DCD) of MnS_2 bilayer to analyze the interlayer electron transfer and further dissect the mechanism of interlayer nonmagnetic atoms stacking-dependent interlayer magnetic coupling. We start from the DCDs of AA stacking and AC stacking which are ferromagnetic antiferromagnetic coupling, respectively, according to Fig. 2(g). Firstly, in all stacking orders, the accumulated electrons mainly reside between interlayer S atoms, so interlayer coupling between layers is bridged by interlayer S atoms through covalent-likely quasibond, which has also been revealed in other 2D materials [45,46]. The binding energy between two layers is also dominated by the interlayer vdW interaction, indicating the significance of interlayer interaction (Supplemental Material, Table S5). The DCDs of MnS_2 bilayer shown in Fig. 3 are also consistent with those of other 1*T*-TMDs [33,47]. However, no obvious s p_z-p_{xy} hybridization [27,28] is observed. Therefore, a new perspective of understanding the interlayer coupling is demanded. In AA stacking, only majority spin (spin up) accumulates at the interlayer region and depletes around the p_z orbits of interlayer S atoms [Fig. 3(a)], indicating that the p_z orbits of interlayer S atoms are simple superposition without forming strong bonding, which follows Pauli exclusion law. As shown in Fig. 3(e), because the interlayer S atoms are staggered along the z direction, the wave functions of p_z orbits contact side by side, leading to simple superposition of the spin-up component, which results in ferromagnetic coupling with the help of intralayer superexchange. In contrast, in AC stacking, both majority spin and minority spin (spin down) accumulate at interlayer region and deplete around p_z orbits of S atoms, suggesting the formation of interlayer bonding [Fig. 3(b)]. In AC stacking illustrated in Fig. 3(f), the interlayer S atoms align along the z direction; the wave functions of p_z orbits contact head to head

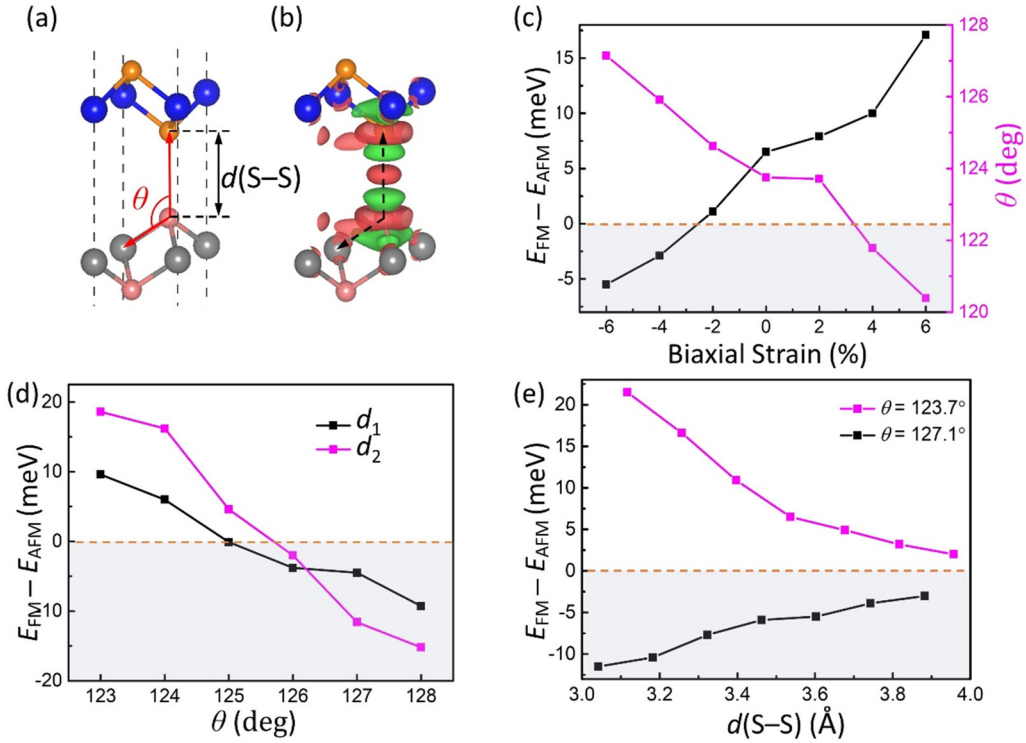

FIG. 4. Strain-tunable interlayer coupling in MnS_2. (a) Interlayer structure of MnS_2 in AA stacking after rotation with defined interlayer distance d (S–S) and interlayer bond angle θ. (b) DCD of bilayer MnS_2 (isosurface value of $0.0001e/\text{bohr}^3$); red and green isosurface contours represent charge accumulation and reduction, respectively. (c) Interlayer coupling energy and interlayer bond angle θ under different biaxial strain. (b) Interlayer coupling energy as a function of interlayer bond angle under two different interlayer distances. (e) Interlayer coupling energy as a function of interlayer distance under two different interlayer bond angles.

and are largely overlapped, resulting in strong bonding at the interlayer. Therefore, both spin-up and spin-down electrons should reside at the interlayer according to Pauli exclusion law and interlayer antiferromagnetic coupling is energetically favored. With rotational transformation, AA^R stacking whose stacking of interlayer S atoms is the same as AC stacking also exhibits similar DCDs as AC stacking indicating, interlayer p_z–p_z bonding, as exhibited in Fig. 3(c). In the same way, AB^R stacking and AA stacking which possess similar stacking of interlayer S atoms and both favor ferromagnetic coupling, have similar spin-dependent DCD, exhibited in Figs. 3(d) and 3(a). We also calculate spin-dependent DCDs of AB stacking and AC^R stacking, which have consistent results (illustrated in Supplemental Material, Fig. S4). In conclusion, a kind of interlayer orbital interaction is found to decide the interlayer coupling in 1T-MnS_2. Whether the interlayer p_z orbital is quasibonded, which is highly relevant to the stacking order of interlayer nonmagnetic atoms, so altering the stacking order leads to different interlayer magnetic coupling. Because we attribute the interlayer coupling directly to the nonmagnetic atoms, we also analyze the magnetic coupling by calculating the interlayer spin-exchange parameters between interlayer S atoms rather than Mn atoms (Supplemental Material, Fig. S6 and Supplemental Material, Table S3 [37]), which exhibit good consistence with the theory we proposed above.

The different magnetic coupling in various stacking orders also leads to alternative band structure. Figures 3(g) and 3(h) present the band structures of MnS_2 in AA stacking and AA^R stacking, respectively. Because monolayer MnS_2 possesses the half-metal band structure with tiny band gap, the band structure experiences the transition between half metal and semiconductor when changing the interlayer magnetic coupling. When two layers are antiferromagnetic coupled, the spin-up and spin-down bands degenerate and exhibit a band gap about 0.2 eV. On the contrary, with ferromagnetic coupling, the spin-up bands from the conduction band and valence band cross the Fermi level and illustrate half-metallic band structure. The alternative stacking order tunes the interlayer magnetic coupling, and further influences the band structure. The band structures of AB, AC, AB^R, and AC^R stacking show the same characteristics as described above (Supplemental Material, Fig. S4 [37]).

Owing to the structural flexibility of 2D materials, we also investigate the influence of biaxial strain on the structure of interlayer nonmagnetic atoms and the resulting variation of interlayer coupling. We take MnS_2 bilayer in AA^R stacking, in which both Mn atoms and interlayer S atoms from two layers are aligned along out-of-plane direction shown in Fig. 4(a) as an example. Figure 4(c) exhibits the evolution of interlayer coupling energy and interlayer Mn–S–S bond angle θ defined in Fig. 4(a) with the applied biaxial strain. The interlayer coupling energy increases monotonically with the strain. Especially, negative strain results in the transition from antiferromagnetic coupling to ferromagnetic coupling. Positive strain, by contrast, enhances interlayer antiferromagnetic coupling. Meanwhile, the interlayer bond angle θ decreases monotonically with the strain, which shows high correlation with the interlayer coupling. From the DCD shown in

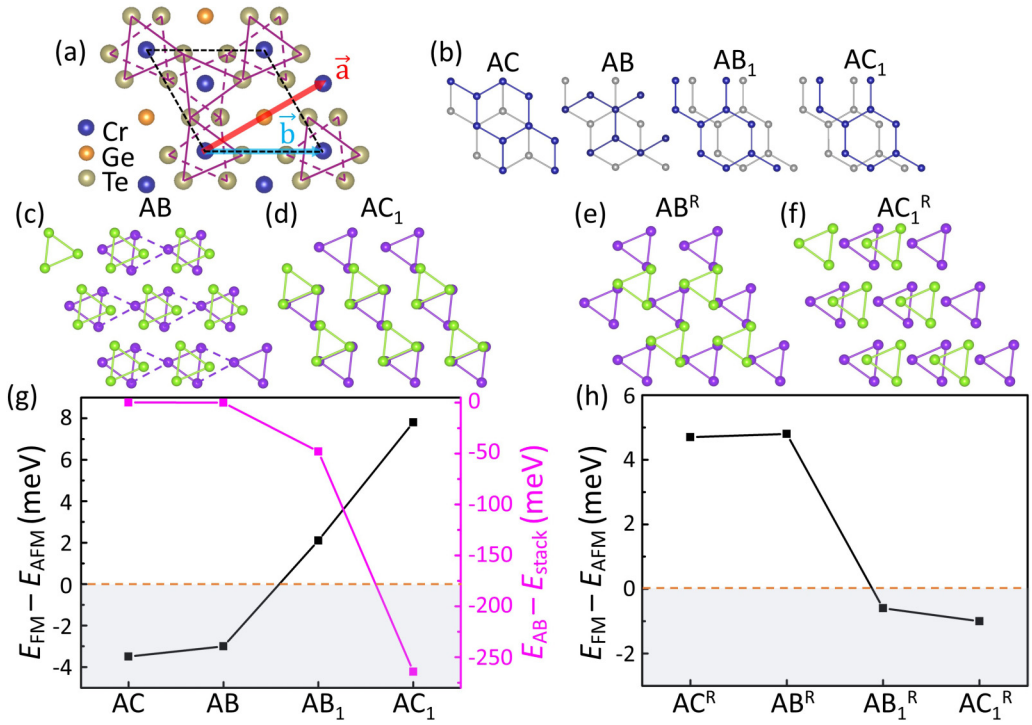

FIG. 5. Stacking-dependent interlayer coupling in $Cr_2Ge_2Te_6$. (a) Top view of $Cr_2Ge_2Te_6$ monolayer. Two shift directions $\vec{a}$ and $\vec{b}$ are labeled as red and blue vectors, respectively. The black dotted rhombuses highlight the primitive cell. (b) Stacking configurations of Cr atoms under various stacking orders. Gray balls and blue balls represent the Cr atoms from bottom and top layer, respectively. (c)–(f) Interlayer structure of Te atoms in (c) AB stacking, (d) AC_1 stacking, (e) AB^R stacking, and (f) $AC_1{}^R$ stacking. Green and magenta balls correspond to lower Te atoms from top layer and upper Te atoms from bottom layer, respectively. (g) Stacking energy and interlayer coupling energy under different stacking orders. (h) Interlayer coupling energy under different stacking orders with rotational transform.

Fig. 4(b), the charge accumulates in two locations, between the interlayer aligned S atoms and between Mn atom and interlayer S atom. Both interlayer distance d (S–S) and the interlayer bond angle θ defined in Fig. 4(a) will contribute to the modulation of interlayer coupling [28,30].

In order to investigate the contribution of θ, we fix the interlayer distance first and investigate the interlayer coupling with different bond angles. As illustrated in Fig. 4(d), under two fixed interlayer distances $d_1 = 3.5$ Å and $d_2 = 3.2$ Å, the interlayer coupling energy shows identical behavior, both decreasing monotonically with θ with essentially the same critical angle. Then we investigate the effect of interlayer distance d on interlayer coupling by fixing the bond angle to two values, $\theta_1 = 123.7^\circ$ and $\theta_2 = 127.1^\circ$; one is smaller than the critical angle while the other is larger. As exhibited in Fig. 4(e), under two fixed θ, the interlayer magnetic configuration shows no sensitivity to interlayer distance under both θ. Meanwhile, the coupling energy both approach 0 when increasing the distance. Therefore, the interlayer distance mostly influences the strength of interlayer coupling. From the discussion above, we come to the conclusion that the bond angle and interlayer distance can effectively affect the interlayer coupling. We also realize that our applied strain is in a moderate range, which can be realized experimentally and does not result in significant change in the interlayer distance. And, the magnetic order can also be changed if the change of interlayer distance is extremely large, such as a few angstrom [33].

The nonmagnetic atom stacking-dependent interlayer coupling can also be applied to other 2D magnetic materials. We take both translational and rotational transformations into consideration and prove that the interlayer coupling is highly related to the stacking of interlayer Te atoms in $Cr_2Ge_2Te_6$ bilayer, which has similar structure to CrI_3. As for translation, we consider two groups of configurations, the shift along two high symmetric directions, $\vec{a}$ and $\vec{b}$ in Fig. 5(a), corresponding to the stacking order of the two phases in CrI_3 [23]. The stacking orders with shift along $\vec{a}$ are referred to as AB and AC; the ones with shift along $\vec{b}$ are referred to as AB_1 and AC_1, exhibited in Fig. 5(b). After the top layer is rotated 180° around Cr site, corresponding stacking orders are named as AB^R, AC^R, $AB_1{}^R$, and $AC_1{}^R$. The lattice constants of all configurations are around 6.88 Å, which only have slight difference from the experimental constant 6.91 Å [4]. From the stacking energy, defined as the energy difference between particular stacking order and the AB stacking order shown Fig. 5(g), the shifting along $\vec{a}$ is more stable than along $\vec{b}$, which is similar to the results in CrI_3 bilayer [27,28] and $CrI_3/Cr_2Ge_2Te_6$ nanostructure [30]. Figures 5(h) and 5(g) also illustrate the interlayer coupling energy under different stacking order with and without rotation, respectively. In line with our expectation, the interlayer coupling alters when shifted to the same stacking order with and without rotational transformation, which is consistent with the results of MnS_2 above. By analyzing the interlayer structure of different stacking,

we find the stacking order of interlayer Te atoms also plays an important role in the determination of interlayer magnetic coupling. The lower Te atoms from the top layer and the upper Te atoms from the bottom layer are aligned along the out-of-plane direction in the AC_1 stacking and AB^R stacking as shown in Figs. 5(d) and 5(e), which both favor antiferromagnetic coupling. By comparison, in AB stacking and $AC_1{}^R$, which possess ferromagnetic coupling, the interlayer Te atoms are staggered along out-of-plane direction and Te atoms from one layer basically occupy the center positions of the triangles formed by the other layer, as illustrated in Figs. 5(c) and 5(f), respectively.

The stacking orders discussed above possess high symmetry, which is derived from the stacking orders of the stable phases in CrI_3, and is demonstrated to be locally the most stable by structural relaxation. The theory obtained from the representative stacking orders with high symmetric structures is also able to explain the situation of more complex stacking [26]. Meanwhile, as shown in Fig. 2, the energy difference among stacking orders is small, indicating the possibility of achieving them in experiment. Therefore, more experimental work is needed to achieve precise control of material preparation with different stacking order and the oxidation of 2D magnets still needs to be solved to expand the application of 2D magnets in devices. At the present stage, the two most common ways for constructing 2D material junctions are exfoliation [48] and molecular-beam epitaxy (MBE) epitaxial growth. As for exfoliation and transfer, the transfer may need to be implemented right after the exfoliation to control the orientation of two layers precisely. As for MBE growth, which is able to obtain metastable states, the exact growth mechanism of 2D magnets still needs to be investigated to realize the flexible control of material growth [49]. Other common methods to control 2D materials, such as pressure, may also be able to cause the phase transition between different stacking orders.

IV. CONCLUSION

In conclusion, by first-principle calculations, we find that in 1T-MnS_2, the interlayer coupling is determined by whether the interlayer p_z orbital is quasibonded, so is tunable by the stacking order of interlayer nonmagnetic atoms. The perspective of the nonmagnetic-atom stacking from which we analyze the interlayer coupling is also applicable in other 2D magnets, which provides the guidance for construction of 2D magnetic heterostructure with different magnetic configurations. In addition, we propose the significant properties of MnS_2, which have great application prospect in spintronic devices. The semiconductor phase can be applied in spin field-effect transistor (FET) which can be regulated by gating, while the semimetal phase which possesses high spin polarization can be utilized as effective spin source. MnS_2, in which the transition between semiconductor and semimetal can be controlled by stacking order and strain, is an excellent platform for the combination of spin FET and spin source.

ACKNOWLEDGMENTS

We are grateful for the support of Beijing Innovation Center for Future Chip (ICFC), Tsinghua University. This work was supported by the National Natural Science Foundation of China (Grant No. 51871130) and the Natural Science Foundation of Beijing Municipality (Grant No. JQ20010).

[1] K. S. Novoselov, A. Mishchenko, A. Carvalho, and A. H. Castro Neto, Science **353**, aac9439 (2016).
[2] Y. Liu *et al.*, Nat. Rev. Mater. **1**, 16042 (2016).
[3] C. Gong, L. Li, Z. Li, H. Ji, A. Stern, Y. Xia, T. Cao, W. Bao, C. Wang, Y. Wang, Z. Q. Qiu, R. J. Cava, S. Louie, J. Xia, and X. Zhang, Nature (London) **546**, 265 (2017).
[4] B. Huang, G. Clark, E. Navarro-Moratalla, D. R. Klein, R. Cheng, K. L. Seyler, D. Zhong, E. Schmidgall, M. A. McGuire, D. H. Cobden, W. Yao, D. Xiao, P. Jarillo-Herrero, and X. Xu, Nature (London) **546**, 270 (2017).
[5] S. Jiang, L. Li, Z. Wang, K. F. Mak, and J. Shan, Nat. Nanotechnol. **13**, 549 (2018).
[6] S. Jiang, J. Shan, and K. F. Mak, Nat. Mater. **17**, 406 (2018).
[7] T. Song, X. Cai, M. W.-Y. Tu, X. Zhang, B. Huang, N. P. Wilson, K. L. Seyler, L. Zhu, T. Taniguchi, K. Watanabe, M. A. McGuire, D. H. Cobden, D. Xiao, W. Yao, and X. Xu, Science **360**, 1214 (2018).
[8] Z. Wang, I. Gutiérrez-Lezama, N. Ubrig, M. Kroner, M. Gibertini, T. Taniguchi, K. Watanabe, A. Imamoğlu, E. Giannini, and A. F. Morpurgo, Nat. Commun. **9**, 2516 (2018).
[9] J. Xiao and B. Yan, 2D Mater. **7**, 045010 (2020).
[10] A. Geim and I. Grigorieva, Nature (London) **499**, 419 (2013).
[11] Y. Zhou, N. Maity, A. Rai, R. Juneja, X. Meng, A. Roy, Y. Zhang, X. Xu, J.-F. Lin, S. K. Banerjee, A. K. Singh, and Y. Wang, Adv. Mater. **32**, 1908311 (2020).
[12] Y. Cao, V. Fatemi, S. Fang, K. Watanabe, T. Taniguchi, E. Kaxiras, and P. Jarillo-Herrero, Nature (London) **556**, 43 (2018).
[13] Y. You and A. Vishwanath, npj Quantum Mater. **4**, 16 (2019).
[14] K. Tran, G. Moody, F. Wu *et al.*, Nature (London) **567**, 71 (2019).
[15] J. Sung, Y. Zhou, G. Scuri *et al.*, Nat. Nanotechnol. **15**, 750 (2020).
[16] K. Serlin, C. L. Tschirhart, H. Polshyn, Y. Zhang, J. Zhu, K. Watanabe, T. Taniguchi, L. Balents, and A. F. Yong, Science **367**, 900 (2020).
[17] S. Carr, S. Fang, and E. Kaxiras, Nat. Rev. Mater. **5**, 748 (2020).
[18] C. Gong and X. Zhang, Science **363**, eaav4450 (2019).
[19] Y. Hou, J. Kim, and R. Wu, Sci. Adv. **5**, eaaw1874 (2019).
[20] F. Lüpke, D. Waters, S. C. de la Barrera *et al.*, Nat. Phys. **16**, 526 (2020).
[21] C. Gong, E. Kim, Y. Wang *et al.*, Nat. Commun. **10**, 2657 (2019).
[22] H. L. Zhuang, P. R. C. Kent, and R. G. Hennig, Phys. Rev. B **93**, 134407 (2016).
[23] M. A. McGuire, H. Dixit, V. R. Cooper, and B. C. Sales, Chem. Mater. **27**, 612 (2015).
[24] T. Song, Z. Fei, M. Yankowitz *et al.*, Nat. Mater. **18**, 1298 (2019).
[25] T. Li, S. Jiang, N. Sivadas *et al.*, Nat. Mater. **18**, 1303 (2019).

[26] W. Chen, Z. Sun, Z. Wang, L. Gu, X. Xu, S. Wu, and C. Gao, Science **366**, 983 (2019).
[27] N. Sivadas, S. Okamoto, X. Xu, C. J. Fennie, and D. Xiao, Nano Lett. **18**, 7658 (2018).
[28] P. Jiang, C. Wang, D. Chen, Z. Zhong, Z. Yuan, Z.-Y. Lu, and W. Ji, Phys. Rev. B **99**, 144401 (2019).
[29] J. Shang, X. Tang, X. Tan, A. Du, T. Liao, S. C. Smith, Y. Gu, C. Li, and L. Kou, ASC Appl. Nano Mater. **3**, 1282 (2020).
[30] C. Long, T. Wang, H. Jin, H. Wang, and Y. Dai, J. Phys. Chem. Lett. **11**, 2158 (2020).
[31] M. Kan, S. Adhikari, and Q. Sun, Phys. Chem. Chem. Phys. **16**, 4990 (2014).
[32] Y. Yue, Mod. Phys. Lett. B **30**, 1650419 (2016).
[33] C. Wang, X. Zhou, L. Zhou, Y. Pan, Z.-Y. Lu, X. Wan, X. Wang, and W. Ji, Phys. Rev. B **102**, 020402 (2020).
[34] K. Hejazi, Z.-X. Luo, and L. Balents, Proc. Natl. Acad. Sci. USA **117**, 10721 (2020).
[35] G. Kresse and J. Furthmüller, Phys. Rev. B **54**, 11169 (1996).
[36] J. P. Perdew, K. Burke, and M. Ernzerhof, Phys. Rev. Lett. **77**, 3865 (1996).
[37] See Supplemental Material at http://link.aps.org/supplemental/10.1103/PhysRevB.103.224404 for more information about the verification of the calculations and data discussion.
[38] S. Grimme, J. Antony, S. Ehrlich, and H. Krieg, J. Chem. Phys. **132**, 154104 (2010).
[39] C. Ling and F. Mizuno, Chem. Mater. **24**, 3943 (2012).
[40] M. Suzuki, B. Gao, K. Koshiishi *et al.*, Phys. Rev. B **99**, 161401(R) (2019).
[41] X.-J. Dong, J.-Y. You, B. Gu, and G. Su, Phys. Rev. Appl. **12**, 014020 (2019).
[42] H.-J. Koo, H. J. Xiang, C. Lee, and M.-H. Whangbo, Inorg. Chem. **48**, 9051 (2009).
[43] M. Bonilla, S. Kolekar, Y. Ma *et al.*, Nat. Nanotechnol. **13**, 289 (2018).
[44] A. Purbawati, J. Coraux, J. Vogel *et al.*, ACS Appl. Mater. Interfaces **12**, 30702 (2020).
[45] J. Qiao, X. Kong, Z. Hu *et al.*, Nat. Commun. **5**, 4475 (2014).
[46] Y. Zhao, J. Qiao, P. Yu, Z. Hu, Z. Lin, S. P. Lau, Z. Liu, W. Ji, and Y. Chai, Adv. Mater. **28**, 2399 (2016).
[47] C. Wang, X. Zhou, Y. Pan, J. Qiao, X. Kong, C.-C. Kaun, and W. Ji, Phys. Rev. B **97**, 245409 (2018).
[48] Y. Huang, Y.-H. Pan, R. Yang *et al.*, Nat. Commun. **11**, 2453 (2020).
[49] J. Dong, L. Zhang, X. Dai *et al.*, Nat. Commun. **11**, 5862 (2020).